Multi-colour reflective metagrating with neutral transparency for augmented reality

Giovanni Magno, Béatrice Dagens, Antonella D'orazio, Olivier Gauthier-Lafaye

Research Article Vol. 32, No. 15 / 15 Jul 2024 / Optics Express 25545
Optics EXPRESS

Multi-colour reflective metagrating with neutral transparency for augmented reality

GIOVANNI MAGNO,[1,*] BÉATRICE DAGENS,[2] ANTONELLA D'ORAZIO,[1] AND OLIVIER GAUTHIER-LAFAYE[3]

[1]Department of Electrical and Information Engineering (DEI), Polytechnic University of Bari, Bari, Italy
[2]Université Paris-Saclay, CNRS, Centre de Nanosciences et de Nanotechnologies, Palaiseau, France
[3]LAAS-CNRS, Université de Toulouse, CNRS, INSA, UPS, Toulouse, France
[*]giovanni.magno@poliba.it

Abstract: This paper presents the design and experimental validation of an all-dielectric and transparent metagrating-based metalens. Leveraging multiple guided mode resonances simultaneously, the metagrating enables the generation of two or more spectrally narrow reflection peaks. These peaks are achieved through the precise engineering of guided mode resonances, allowing for the reflection of a comb of vibrant and saturated colours. In addition to the investigation of underlying mechanisms, we introduce an analytical numerical method that facilitates rapid engineering of the spectral positions of the reflection peak comb. Experimental validation is provided for a bichromatic sample. Such metagrating can be promising for augmented reality systems, supporting individuals with mild to moderate cognitive impairments by delivering visual and textual stimuli that can improve indoor navigation, home safety, communication, and decision-making.

1. Introduction

The escalating linear progression in the average global age is emerging as one of the most significant societal challenges of the current century [1]. Novel technological solutions aimed at improving quality of life have the potential to mitigate the natural decline in functional, physical, and cognitive abilities that come with aging. Certain areas of application hold significant importance in fostering "active and healthy" aging of people in one's own environment. These areas, such as those pertaining to the autonomy, mobility, and safety of the elderly and/or frail individuals, must also uphold their privacy and individual dignity.

Technologies based on electromagnetic fields carry substantial potential for augmenting quality of life. Radiofrequency and optical frequency systems have the potential to significantly enhance the widespread availability of connections. They can be highly valuable for implementing localization and navigation systems, as well as for sensitive components. It's worth noting that optical frequencies in the visible spectrum are safe for human eyes when used at appropriate power levels. These frequencies can serve multiple purposes, including illumination, information display, and communication, as demonstrated by technologies like LiFi systems.

Within this context, the development of new human-machine interfaces (HMIs) holds pivotal importance, acting as direct intermediaries between information-producing systems and users themselves. HMIs prove particularly valuable in instances of cognitive impairment and sensory loss [2,3]. Specifically, for cognitive impairment cases [4], the ability to present visual information in a clear and effective manner (e.g., aiding indoor navigation by indicating directions or hazards for home safety) offers significant support to individuals dealing with such conditions [5–7]. This visual information fosters comprehension and decision-making, even amidst varying degrees of cognitive impairment, which could otherwise substantially deteriorate their quality of life unless adequately supported or compensated.

#520430 https://doi.org/10.1364/OE.520430
Journal © 2024 Received 31 Jan 2024; revised 20 Mar 2024; accepted 20 Mar 2024; published 2 Jul 2024

Optics EXPRESS

Augmented reality (AR) displays offer an innovative means of presenting visual information to observers. These displays enable individuals to view images, symbols, and text overlaid onto the entire "natural" scene in which they are situated and engaged. Utilizing visual and visual-textual cues, such as photos, memory books and wallets, reminder cards, pictograms, video content, and other visual tools, can significantly enhance word-finding and communication capacity during conversations [8]. These aids also hold the potential to enhance decision-making abilities, particularly in cases of mild to moderate dementia [9]. Besides, such systems are of paramount interest to a plethora of different applications, ranging from Industry 4.0 [10], to vehicle driving aids [11,12], to defence.

An AR system relies on a support surface or surfaces, i.e. eyeglass lenses, a windshield, a helmet visor, etc., which must possess specific qualities. These surfaces need to be both reflective for specific wavelengths and transparent for the rest of the visible spectrum. This unique combination ensures that the desired information can be presented to the observer without compromising the overall brightness or colour perception of the surrounding scene. At the heart of the near-eye display, this surface is properly tilted or shaped and attached to a rigid wearable support, such as eyeglass frames (see Fig. 1(a)). Additional optical elements can also be incorporated for manipulating the light path (i.e., magnification, steering, etc.). Subsequently, the visual information is projected onto this display using either a laser projector or an LCD display.

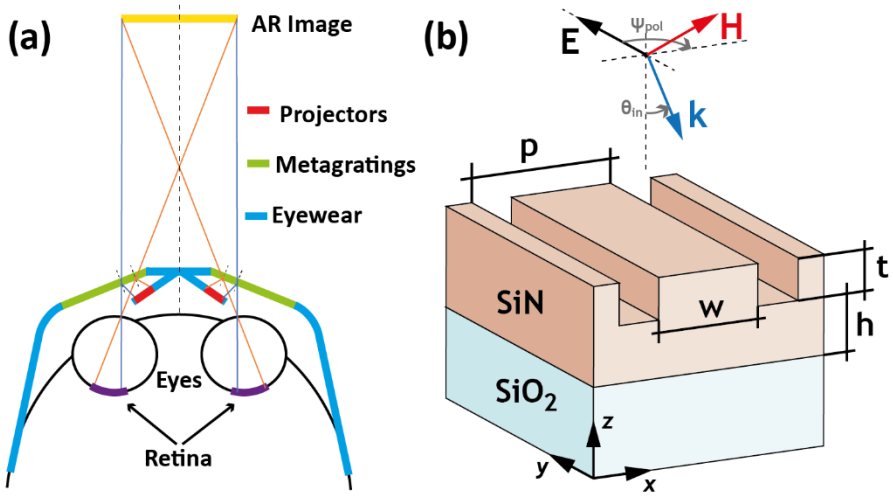

Fig. 1. (a) Conceptual architecture of an AR visor. A projected image is reflected by a metagrating to form a retinal image. (b) Sketch of the proposed metagrating.

In 1968, Ivan Sutherland created his inaugural head-mounted AR prototype [13], famously known as the "Sword of Damocles" due to its considerable weight and the fact that a section of it was suspended from the ceiling. Since that time, various systems featuring progressively reduced sizes, lighter weights, and improved wearability have been introduced [14,15]. While numerous companies and research centres are unveiling their respective systems, the quest for an ideal design remains ongoing. Achieving the perfect, natural vision without causing any user discomfort necessitates the optimization of multiple parameters simultaneously, presenting a formidable challenge that is still in need of a suitable solution. Certainly, an ideal display should possess several key attributes. It should be compact, lightweight, comfortable to wear, have high brightness and an ample colour expression capacity, while also offering high resolution, a wide field of view and eyebox, and the absence of the vergence-accommodation conflict [16]. Visual acuity refers to the capacity to perceive and distinguish small details with the naked eye. Regardless of the distance separating the screen from the eye, achieving an equivalent

Optics EXPRESS

level of acuity as that of a person with 20/20 vision necessitates a resolution of 1 arcminute, equivalent to a display resolution of 60 pixels per degree. Near-eye displays can be designed by exploiting various approaches, including waveguides [17–19], refractive freeform optics [20,21], metasurfaces [22,23], pinlight [24], holography, transmissive mirror devices, and even through combinations of these methodologies.

In this paper, our primary emphasis will be on metasurface-based near-eye display. Metamaterials offer extraordinary control over electromagnetic waves interacting with them, both in terms of angle and spectral characteristics. Whether composed of purely dielectric [25–27] or plasmonic [28–34] materials, meta-atoms constituting the fundamental building blocks of metamaterials enable unmatched manipulation of electromagnetic wavefront on a scale comparable to or smaller than the wavelength. In a similar manner, metasurfaces, which are two-dimensional counterparts of metamaterials, hold the potential to overcome the angle-spectral constraints of conventional refractive surfaces while offering significantly smaller form factors. Furthermore, metasurfaces can be effectively combined with other techniques and tools such as nanoantennas [35,36], mode coupling [37–40], guided-mode resonances [41], Pancharatnam–Berry phase [42], freeform optics [43]. This combination enables such arbitrary manipulation of the optical wavefront in new ways. One notable example is the metaform paradigm, which seamlessly integrates metasurfaces and freeform optics into a single, compact optical device [44,45].

To effectively support individuals with medium to severe cognitive deficits, a near-eye display must possess the capability to selectively reflect a minimum of two colours. For example, red visual-text stimuli can be projected to represent negative, prohibition, or danger-related cues, while green stimuli can be used for positive, permission, or reassurance-related information. Additionally, the display should allow the remaining part of the light spectrum to pass through unaltered, ensuring sufficient transparency and chromatic neutrality so as not to distort colour perception of the scene.

To engineer the spectral response and design a metasurface with reflection peaks precisely centred at wavelengths corresponding to primary colours, we aim to leverage the paradigm of guided-mode resonances (GMR) [46].

In the context of near-eye display design, a diffraction grating positioned close to a waveguide acts as a phase adapter between the incident wave and the mode supported by the guide, enabling the excitation of guided modes by direct illumination. This interaction leads to resonances arising due to the coupling between the diffracted fields from the grating and the leaky modes that can house within the effective waveguide. GMR-based filters (GMRF) have proven especially effective in customizing the transmission characteristics of an interface. Structures supporting GMRs enable the design of multi-colour filters characterized by a very narrow linewidth and high efficiency. So far, single colour GMR-based reflecting filter exploiting 1D dielectric gratings have been proven valuable [47–49]. Moreover, structures supporting multiple GMRs have been demonstrated in the NIR spectral domain by exploiting either multimode waveguides [50] or 2D crossed gratings [51]. Multiresonant metasurfaces can be also attained by exploiting coupled high-order multipoles in dielectric nanoresonators, as recently shown in [52].

2. Methods and structure

Here we propose a transparent metasurface, specifically a metagrating, that supports multiple guided mode resonances in the visible spectrum and can selectively reflect two or more colours simultaneously. Figure 1(a) illustrates a conceptual architecture for an AR visor. The core element is a lens housing, partially or fully incorporating a tilted metasurface (light green lines). This assembly is mounted on a rigid frame (light blue lines) designed for comfortable wear like eyeglasses. The system enables binocular viewing of a virtual image (yellow line). A directional light source on the frame projects the image onto the lens. The reflected light then forms the virtual image on the user's retinas. The challenges lie in simultaneously engineering multiple

Optics EXPRESS

guided resonances and determining the optimal geometry to ensure concurrent and uniform colour selection. The paper will begin with an introduction to the geometry and materials that define the structure. Subsequently, both analytical and numerical analyses will be discussed to delve into the underlying mechanisms and determine the relevant degrees of freedom for engineering. Simulations were initially carried out using the 3D Finite-Difference Time-Domain (FDTD) method, by which we investigated the behavior of the structure as the different degrees of freedom involved were varied. Then, design criteria were defined, and potentially optimal configurations were determined through a numerical-analytical approach based on resolving the equation governing guided resonance phenomena. Subsequently, these configurations have been further examined by using the 2D Rigorous Coupled-Wave Analysis (RCWA) method, which is computationally efficient and in good agreement with 3D FDTD simulations. Specifically, the publicly available software RETICOLO [53] was utilized for these investigations. Finally, the experimental demonstration will be presented, providing insights into both the fabrication process and the outcomes of the experimental characterization.

Figure 1(b) shows a sketch of the structure: it consists of the stacking of an asymmetric waveguide, composed of a h-thick SiN film ($n_{SiN} = 2$) on a SiO_2 substrate ($n_{SiO2} = 1.5$), and a 1D subwavelength grating, composed of t-thick SiN ridges having width w and period p. The air superstrate ($n_{air} = 1$) introduces an asymmetry in the waveguide along the z-direction due to its differing refractive index from the substrate. The structure is excited by a plane wave with an incidence angle θ_{in} in the xz-plane with respect to the metasurface normal plane. The polarisation forms an angle ψ_{pol} in the xy-plane with respect to the y-axis, as shown in the sketch. To simplify fabrication, the thickness t of the SiN ridges is set equal to 100 nm.

3. Results and discussion

Firstly, the behaviour of the metasurface was studied as a function of the individual geometric parameters. Specifically, we investigate the independent effects of the grating thickness t, duty cycle dc (defined as 100 w/p), polarization angle, and incidence angle on the reflectance and transmittance of the metasurface in the spectral window between 400 and 900 nm. For each simulation series, a single parameter was varied at a time, while the remaining geometric parameters were fixed as follows: $h = 100\,nm$, $p = 322\,nm$, $dc = 60\%$ (i.e., $w = 0.6{\times}p$), $\theta_{in} = 0°$, and $\psi_{pol} = 0°$. At this stage of the investigation, we want the effective guiding core (composed of the continuous SiN layer and the SiN grating) to support a single mode and give rise to a single guided mode resonance. This justifies the initial choice of h.

In gratings, the component of the incident wave vector, $k_{||,i}$, that is parallel to the grating plane must remain conserved in the transmitted or reflected wave vector, except for integer multiples m of the grating vector, $k_p = 2\pi/p$ [54]. Similarly, in the case of a coupled diffraction grating - waveguide system, as in the proposed structure, the excitation of a leaky propagating mode with propagation constant β_m occurs when the condition $k_{||,i} = \beta_m$ - mk_p is satisfied. Consequently, this implies that the effective refractive index of the excited mode must satisfy the following equation:

$$n_{eff} = n_i \, sin(\theta_{in}) + m\frac{\lambda}{p} \tag{1}$$

where n_i represents the refractive index of the medium through which the incident wave propagates (in our case, the air, with n_i =1). When this condition is met, it results in the emergence of guided mode resonance, which manifests as a peak in the reflectance of the metasurface. For instance, for the geometry previously set ($t = 100\,nm$, $h = 100\,nm$, $p = 322\,nm$, $dc = 60\%$, $\theta_{in} = 0°$, and $\psi_{pol} = 0°$), a reflection peak, with an intensity close to the unit, appears close to 542 nm. In these conditions, to attain a guided-mode resonance, the mode effective refractive index must be $n_{eff} = \lambda/p \approx 1.68$. This value is in good agreement with the effective refractive index of the fundamental TE mode, which is calculated analytically to be 1.69 in a four-layer waveguide

Optics EXPRESS

configuration. In this calculation, the refractive index of the grating layer is modelled as a weighted average of silicon nitride and air refractive indices, determined by their respective widths within the structure (i.e., $p/w \times n_{SiN} + (p\text{-}w)/p \times n_{Air} = 0.6 \times 2 + 0.4 \times 1 = 1.6$).

Figure 2 shows the reflection maps of the metasurface as a function of wavelength and for each geometric parameter. In particular, in Fig. 2(a), (b), (c), (d) and (e), the reflection maps are obtained by varying the grating thickness, duty cycle, incidence angle, polarization angle, and period, respectively. Figure 2(a) shows that with a t thicker than 150 nm, a second resonant mode arises and is spectrally positioned at lower wavelengths. Therefore, choosing $t = 100\,nm$ corresponds, under these conditions, to the presence of a single reflection peak with an amplitude near to unity. Figure 2(b), on the other hand, shows a reflection peak with an amplitude near to unity for dc values ranging from 50% to 75%. However, we fixed this value to 60% to avoid the spacing between the SiN ridges becoming too narrow and resulting in possible fabrication issues. Figure 2(c) shows that for an incidence angle different from zero, the resonance splits into two distinct "branches" due to the removal of the degeneracy of the forward- and backward-propagating modes that propagate in the guide-diffraction grating system under these excitation conditions. The upper branch (co-propagating) in particular exhibits a spectral shift towards red as the incidence angle increases. The lower branch (counter-propagating), on the other hand, blueshifts. In Fig. 2(d) we observe that, by increasing the polarization angle between 0 and 90°, the resonance at about 525 nm weakens and another one at about 550 nm appears simultaneously. This is caused by the system's TE modes only being excited for $\psi_{pol} = 0°$ and TM modes only being excited for $\psi_{pol} = 90°$, respectively, while for intermediate angles there is a combination of variable intensities of the two groups of modes. Finally, Fig. 2(e) shows that, when p increases between 200 and 500 nm, a single reflectance peak redshifts at a rate of about 1.3 nm for every 1 nm increase in period. Furthermore, Fig. 2(e) illustrates the colour palettes perceived in reflection and transmission spectra, the derivation of which will be explained later. These palettes demonstrate the potential to achieve a broad range of colours, with vibrant and saturated hues in reflection and subtle and highly desaturated shades in transmission. This aspect is of paramount importance as the metasurface should not distort the colour perception of the scene observed through it.

Having established the impact of individual parameters on the guided mode resonance, our aim is to leverage the coexistence of multiple guided modes to achieve multiple reflectance peaks at desired wavelengths and for a $\theta_{in} > 0°$. Specifically, our goal is to identify two types of solutions: bichromatic solutions that simultaneously maximize the structure's reflectance around the wavelengths of green and red, and trichromatic solutions that achieve this across blue, green, and red wavelengths simultaneously.

To determine the wavelengths that best yield the visual response for blue, green, and red, we firstly hypothesize a reflectance function, R, that approximates a single peak with a Gaussian distribution given by:

$$R(\lambda) = exp\left(-\left(\frac{\lambda - \lambda_0}{\sigma}\right)^2\right), \tag{2}$$

where λ represents the working wavelength, λ_0 is the wavelength at which the reflectance is maximized, σ is a parameter associated with the full width at half-maximum (in wavelengths) $\Delta\lambda$ derived from the relationship $\Delta\lambda = 2\sigma\sqrt{(\log(2))} \approx 1.665\sigma$.

Given $R(\lambda)$, it is possible to calculate the associated CIE 1931 XYZ tristimulus function [55] and subsequently the corresponding RGB colour. A good approximation of the three primary colours is obtained by selecting λ_0 as $\lambda_B = 442\,nm$ (blue), $\lambda_G = 542\,nm$ (green), and $\lambda_R = 641\,nm$ (red), respectively, with $\sigma = 45\,nm$ ($\Delta\lambda = 75\,nm$). It is worth to point out that, for narrower spectra, rendering the blue requires a larger centre wavelength (about 465 nm when $\Delta\lambda < 30\,nm$). Since we expect guided mode resonances to be particularly narrow, without loss of generality we consider a wavelength for blue of $\lambda_B = 465$ nm. For the near-eye display application, we will

Optics EXPRESS

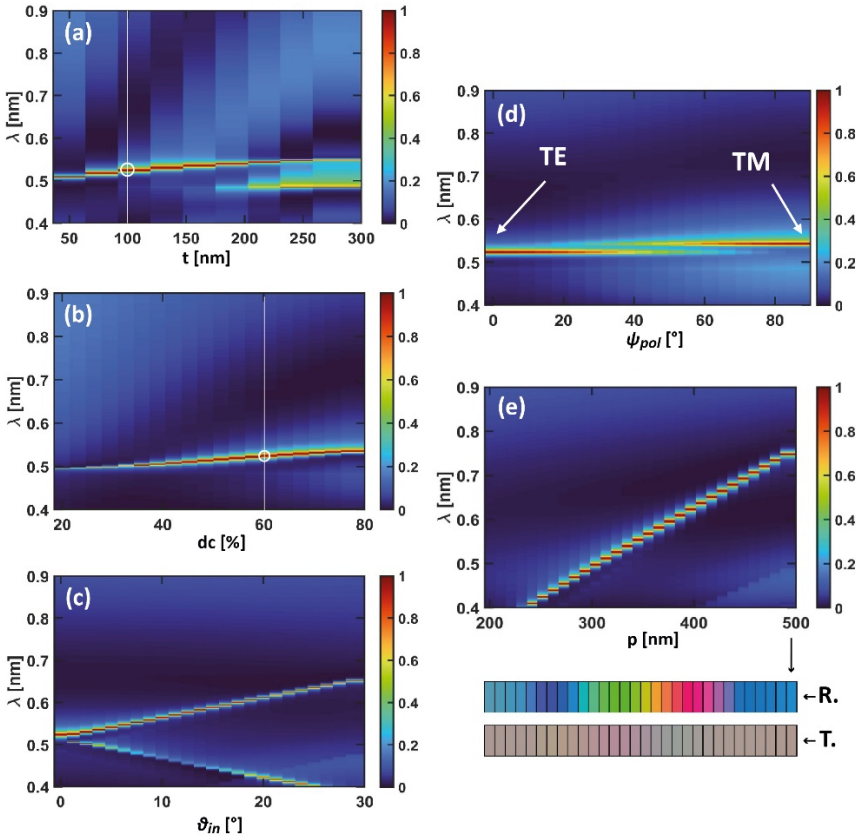

Fig. 2. Metasurface reflectance as a function of the wavelength and of the (a) grating thickness, (b) duty cycle, (c) incidence angle, (d) polarization angle, and (e) period. In (e), corresponding colours for the reflectance and the transmittance are shown as a function of the period.

consider the colour saturation acceptable if it is at least equal to that of the corresponding primary colour (i.e., $\Delta\lambda \leq 75\,nm$).

As the period p and thickness h vary, we systematically searched for solutions to Eq. (1) as a function of λ. This involved identifying all points of intersection between the linear equation on the right side of Eq. (1) (i.e., $n_i \sin(\theta_{in}) + m\lambda/p$) and the effective refractive indexes n_{eff} of the TE and TM modes supported by the structure and retrieved analytically as previously explained. To ease the identification of the desired bichromatic and trichromatic solutions, a cost function F has been established.

F is defined as the sum of the minimum distances between the wavelengths of the solutions obtained from Eq. (1), λ_{res}, and the target wavelengths $\lambda_n = (\lambda_B, \lambda_G, \lambda_R)$. Let F_2 and F_3 be the cost functions for the bichromatic and trichromatic cases, respectively, defined analytically as follows:

$$F_2 = \Sigma_{n=(G,R)}\, min||\lambda_{res} - \lambda_n||, \tag{3}$$

$$F_3 = \Sigma_{n=(B,G,R)}\, min||\lambda_{res} - \lambda_n||. \tag{4}$$

Figure 3 shows the logarithm of the cost function F_3 for trichromatic design in the case of TM modes (a similar map is obtained for TE modes, where the minima are slightly shifted towards

Optics EXPRESS

smaller periods and thicknesses) calculated as a function of the period p and of the thickness h, when $\theta_{in} = 45°$ and $m = -1$.

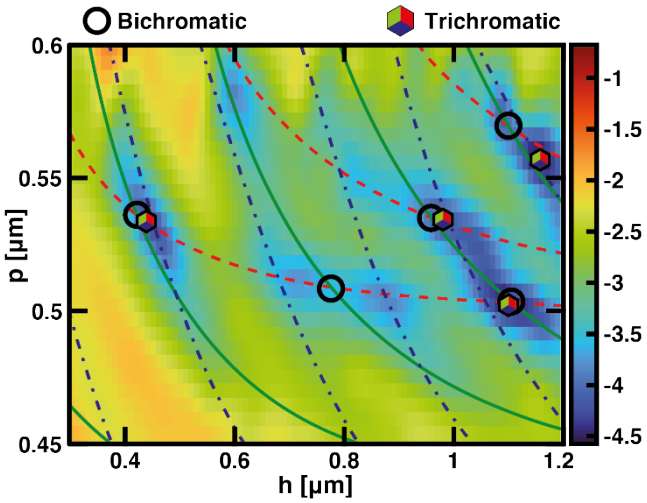

Fig. 3. Logarithm of the cost function F_3 for TM modes as a function of p and h, when $\theta_{in} = 45°$. The points corresponding to the intersections of the green and red loci (bichromatic solutions), and those that, by minimizing the cost function F_3, minimize the distances between the blue, green, and red loci (trichromatic solutions), are highlighted with dedicated markers.

To ease the interpretation of the cost function, the loci of solution ensuring the existence of a guided mode resonance at the desired wavelengths are superimposed (dashed red curves, solid green curves, and dash-dot blue curves indicate resonances occurring at λ_R, λ_G, and λ_B, respectively). The points corresponding to the intersections of the green and red locations (bichromatic green-red solutions, minimising F_2), as well as those minimizing the distance between the blue, green, and red locations (trichromatic solutions) by minimising F_3, are highlighted using distinct markers.

Table 1 provides values for the period of the metasurface and the thickness of the SiN layer for the identified minima in the trichromatic cost functions for TM polarization (as shown in Fig. 3) when $\theta_{in} = 45°$. In addition, for each solution identified, the following table shows an ID, the corresponding value of the logarithm of the cost function and the relative distances $\Delta\lambda_B$, $\Delta\lambda_G$ and $\Delta\lambda_R$ between the expected resonances and the desired wavelengths. It is worth noting that, a trichromatic solution includes a bichromatic one.

Table 1. TM trichromatic solutions with lowest *F* obtained by numerically solving Eq. (1) for $\theta_{in} = 45°$

ID	p [nm]	h [nm]	log(F_3) [arb.u.]	$\Delta\lambda_B$ [nm]	$\Delta\lambda_G$ [nm]	$\Delta\lambda_R$ [nm]
$A_{3,TM}$	557	1160	-4.36	0.7	2.9	-4.9
$B_{3,TM}$	534	440	-4.0	-4.9	4.23	1.2
$C_{3,TM}$	534	980	-4.0	-8.3	3.55	1.3
$D_{3,TM}$	502	1100	-4.25	-0.7	-1.2	-0.9

The most promising TM configurations among these candidates were examined using the RCWA method, where reflectances were determined within a vicinity of the periods and thicknesses reported in Table 1.

Optics EXPRESS

For the most compact solution in terms of period and thickness, $B_{3,TM}$, the RCWA analysis yielded an optimised configuration at $p = 530\,nm$ and $h = 452.5\,nm$. Figure 4 shows the TM reflectance map as a function of the wavelength and of h (between 0 and 1 μm), when $p = 530\,nm$. For h values below 0.2 μm, a single reflectivity peak is found, which redshifts as h increases. For an increasing h greater than 0.2 μm, an increasing number of reflectance peaks arise and redshift, reflecting the presence of an increasing number of guided modes in the structure. For $h = 452.5\,nm$ (corresponding to the horizontal white solid line in Fig. 4), three distinct reflectance peaks are observed crossing the 10 nm-wide tolerance regions located in the vicinity of the target wavelengths.

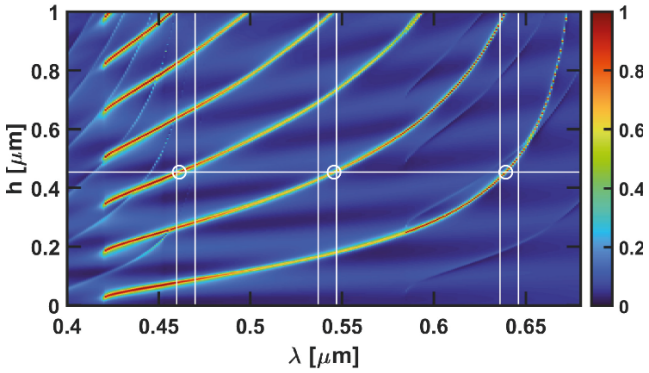

Fig. 4. Reflectance of the proposed structure as a function of wavelength and of the thickness h, when $p = 530\,nm$, for $\theta_s = 45°$ and for the TM polarisation. Vertical white lines delimit a tolerance interval of 10 nm around the wavelengths corresponding to blue, green, and red colours, while the horizontal white solid line highlights $h = 452.5\,nm$. The circular markers highlight the intersections between the resonant peaks and the horizontal line.

To shed light on the nature of these peaks, we present in Fig. 5 a comparative analysis involving the effective refractive indices of the modes supported by the structure. These are obtained through the analytical calculation method described earlier, applied to three distinct thicknesses of the homogeneous SiN layer (namely, 385 nm, 435 nm, and 485 nm). In particular, the clusters of light blue, red, and green curves represent, respectively, the dispersion curves of the TM_0, TM_1, and TM_2 modes. These modes display one, two, and three maxima in the distribution of the magnitude of the magnetic field within the effective core of the waveguide-grating system.

In Fig. 5, the n_{eff} required to have guided mode resonances (Eq. (1), when m = 1) for three different periods (509 nm, 534 nm, and 559 nm, respectively) are superposed. Moreover, for the 534 nm period, the yellow and violet solid lines correspond to the n_{eff} calculated when m = -2 and -3, respectively. The circular markers highlight the intersections between the calculated dispersion curves (continuous lines) when $h = 435\,nm$ and the black curve indicating the required n_{eff} for resonant behaviour at $p = 534\,nm$ and $m = 1$. Similarly, small asterisk-shaped markers are placed at the intersections with the diffraction order curves m = -2 and -3. The analytical results depicted in Fig. 5 exhibit complete consistency with the numerical outcomes presented in Fig. 4. The highlighted intersection points in Fig. 5 remarkably predict the resonant peaks observed in Fig. 4, including those attributed to the diffraction orders m = -2 and -3. As evident in Fig. 4, these secondary and less intense peaks occur for wavelengths respectively exceeding about 575 nm and shorted than about 460 nm. Furthermore, a distinct trend is clear in Fig. 5: resonances redshift with an increase in either the core thickness or the period of the structure. Similarly to what was done for configuration $B_{3,TM}$, for the remaining configurations, the RCWA analysis provides the optimized values of period and core thickness, which are reported in Table 2. For solutions $C_{3,TM}$

Optics EXPRESS

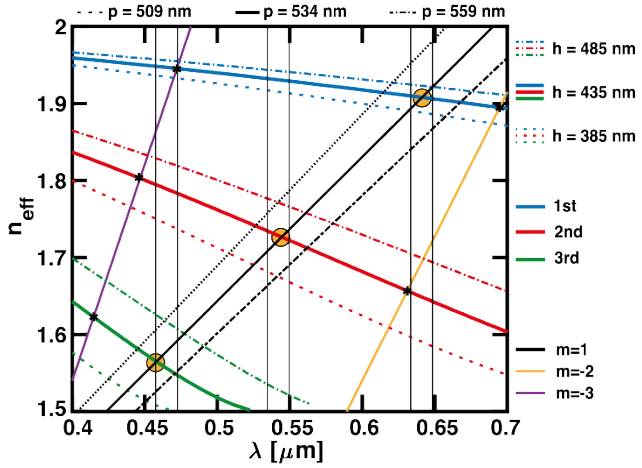

Fig. 5. (light blue, red, and green curves): Dispersion curves of TM modes supported by the structure for $h = 385\,nm$ (dashed lines), $435\,nm$ (solid lines), and $485\,nm$ (dash-dot lines), respectively. (set of black lines, and yellow and violet lines): Values of n_{eff} from Eq. (1) for $m = 1$ (black lines), and for $m = -2$ (yellow line) and $m = -3$ (violet line), respectively. The black lines correspond to $p = 509\,nm$ (dashed line), $534\,nm$ (solid lines), and $559\,nm$ (dash-dot line), respectively. The intersections between curves for $h = 435\,nm$ and $p = 534\,nm$, which correspond to the guided resonances predicted in Fig. 4, are indicated by circular ($m = 1$) and star ($m = -2$ and -3) markers. Vertical black lines delimit a tolerance interval of $10\,nm$ around the wavelengths corresponding to blue, green, and red colours.

and $A_{3,TM}$ the RCWA analysis yielded an optimised configuration at $p = 535\,nm$, $h = 997.5\,nm$ and at $p = 562.5\,nm$, $h = 1140\,nm$, respectively.

Table 2. Optimized trichromatic configurations obtained through RCWA analysis, starting from those identified in Table 1

ID	p [nm]	h [nm]	$\Delta\lambda_B$ [nm]	$\Delta\lambda_G$ [nm]	$\Delta\lambda_R$ [nm]
$A_{3,TM}$	562.5	1140	-1.0	2.4	-0.9
$B_{3,TM}$	530	455	-3.4	4.3	-1.7
$C_{3,TM}$	535	997.5	-5.4	6.1	3
$D_{3,TM}$	502.5	1102.5	-1.2	-1.4	-0.5

Finally, the performance of the optimized metalenses is presented. We here analyse the reflectance and the corresponding chromatic perception obtained by selectively illuminating the metasurface with a narrowband beam centred on the reflectance peaks. Additionally, the transparency of the metalens for normal incidence will be examined. The configurations will be presented in order of decreasing compactness, starting with the one with the smallest core thickness of the waveguide and corresponding to a smaller number of guided modes or guided mode resonances. The reflectance and transmittance spectra corresponding to the optimized $B_{3,TM}$ solution are depicted in Fig. 6. The three distinct reflectance peaks (accompanied by transmittance minima) are positioned at $461.6\,nm$, $546.3\,nm$, and $639.3\,nm$, with amplitudes of 93%, 75%, and 97%, respectively. The linewidths (full width at half maximum) of the corresponding resonances are about $5.6\,nm$, $3.7\,nm$ e $1.5\,nm$, respectively. The distances between the peak positions and the target wavelengths are $\Delta\lambda_B = -3.4\,nm$, $\Delta\lambda_G = 4.3\,nm$, and $\Delta\lambda_R = -1.7\,nm$. The figure also includes the CIE chromaticity diagram, highlighting the positions of the perceived

Optics EXPRESS

colours B, G, and R when the structure is illuminated with a source centred on each resonant peak and having a spectral width of 20 *nm*. On the same diagram, the positions of the three primary colours (vertices of the overlaid triangle) and the standard white D65 point (white circle) are marked. Additionally, the perceived colour in transmission T, when the metasurface is illuminated at normal incidence by a standard white D65 source, is denoted by a black dot. This behaviour is particularly suitable for near-eye lens implementation because, in addition to the peaks enabling reflection of blue, green, and red colours, it doesn't substantially alter the colour perception of the visual field observed through the lens.

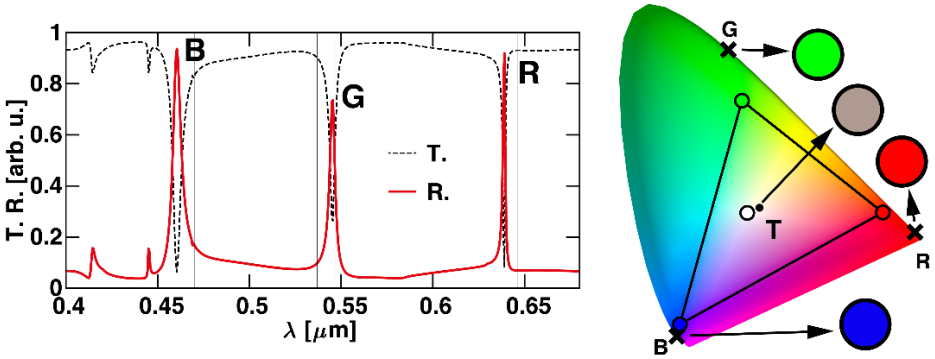

Fig. 6. (left): Transmittance and reflectance when $p = 530\,nm$ and h = 452.5 *nm*, under TM polarization and 45° incidence. (right): CIE chromaticity diagram illustrating the positions of the colours perceived in reflection when metasurface is illuminated by a 20 *nm* width source at resonance peaks. The vertices of the overlaid triangle denote the three primary colours, while the D65 white point marked by white circle. The perceived colour position in transmission (black dot) is shown when the metasurface is illuminated at normal incidence by a standard D65 white light source.

Figure 7 displays the reflectance and the transmittance for the optimized configurations $A_{3,TM}$ and $C_{3,TM}$. These designs exhibit polychromatic behaviour, capable of reflecting a set of distinct colours. In configuration $A_{3,TM}$, as shown in Fig. 7(a), the 6 peaks are located at wavelengths of 464 *nm*, 501.5 *nm*, 544.5 *nm*, 591.5 *nm*, 640 *nm*, and 683.5 *nm*, with intensities of 94%, 86%, 73%, 80%, 64%, and 97%, respectively. In configuration $C_{3,TM}$, as shown in Fig. 7(a), the 7 peaks are positioned at wavelengths of about 425.5 *nm*, 459.5 *nm*, 501 *nm*, 548 *nm*, 598 *nm*, 644 *nm*, and 678.5 *nm*, with intensities of 94%, 98%, 72%, 73%, 78%, 97%, and 93%, respectively. Finally, configuration $D_{3,TM}$ (not shown) displays 8 peaks, located at wavelengths of 402 *nm*, 430.5 *nm*, 464 *nm*, 501 *nm*, 540.5 *nm*, 580 *nm*, 615.5 *nm*, and 640.5 *nm*, with intensities of 95%, 98%, 76%, 68% 83%, 85%, 96%, and 95%, respectively.

An experimental demonstration of the metalens was achieved through the fabrication of a bichromatic configuration, having a desired grating period $p = 680\,nm$ and a target core thickness $h = 635\,nm$. Without loss of generality, this configuration was chosen both for ease of fabrication due to the relatively large period and because it features, for both the TE and TM modes, two reflectance peaks near green and red wavelengths. Specifically, a sample with an area of 0.5×0.5 mm^2 was manufactured via ICP-PECVD (inductive-coupled-plasma plasma-enhanced chemical vapor deposition) of a SiN layer on a SiO_2 substrate. The grating pattern was then etched using a standard process involving electron beam lithography followed by dry etching using CHF_3-based chemistry. The measured thickness of the deposited layer is 747 *nm*, while the measured etching thickness is 102 *nm*, resulting in a fabricated core thickness of 645 *nm*.

The sample was characterized using an EP4 Accurion imaging ellipsometer. Initially, the dispersive refractive index of the SiN layer was measured. Subsequently, we conducted

Optics EXPRESS

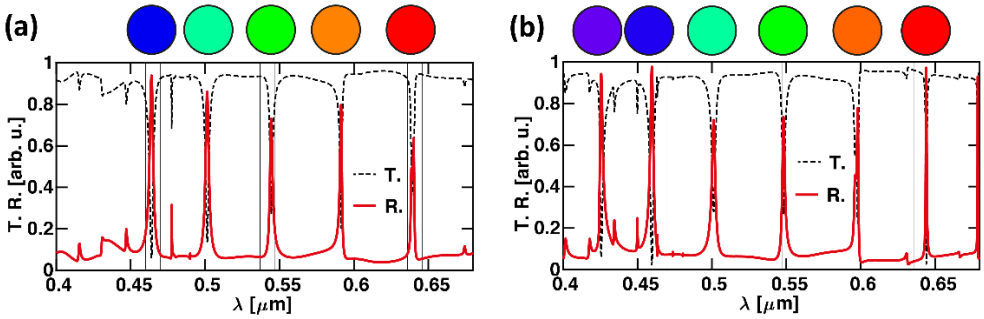

Fig. 7. Transmittance and reflectance calculated when considering configurations (a) $A_{3,TM}$ and (b) $C_{3,TM}$, under TM polarization and 45° incidence. The circles placed above the peaks indicate the calculated perceived colour in reflection when illuminating the metasurface with a spectrally wide 20 nm source centred on the corresponding peak.

measurements of the reflectance under oblique incidence and the transmittance at normal incidence with respect to the sample on an area of $80 \times 80\,\mu m^2$. Reflectance measurements were normalized to the reflectance of a 200 *nm* thick gold layer deposited on silicon. For the transmission experiments, normalization was performed by comparing the results to the signal obtained without the sample. The experimental results were compared with RCWA simulations, considering the actual thicknesses of the sample and the measured dispersion of SiN (shown in the inset of Fig. 8(a)). Figure 8(a-c) shows the comparison between measurements and simulations for angles of incidence of 45° and 50° and for TE and TM polarizations.

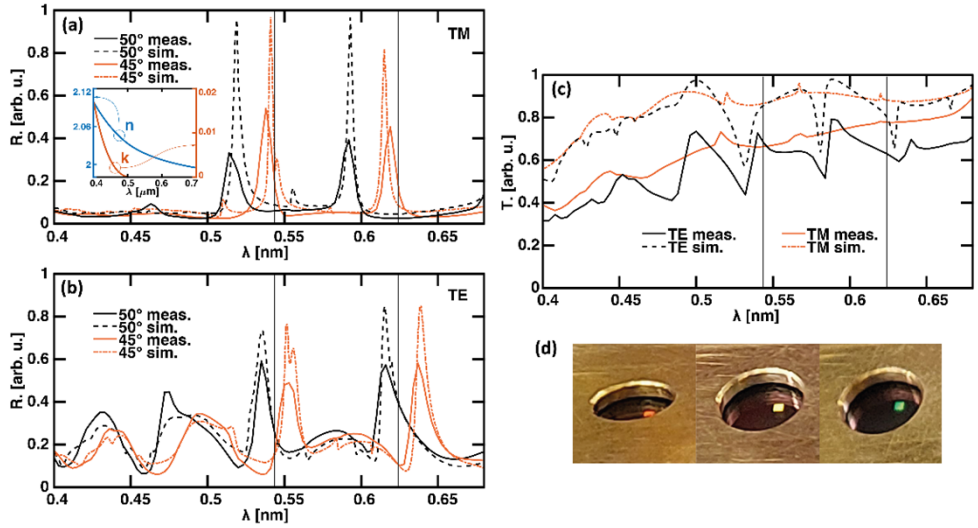

Fig. 8. (a,b) Experimental (solid curves) and simulated (dashed and dot-dashed curves) reflectance obtained for (a) TM and (b) TE polarization and for an angle of incidence of (orange curves) 45° and of (black curves) 50°. (inset) measured refractive index and extinction coefficient of SiN. (c) Experimental (solid curves) and simulated (dashed and dot-dashed curves) transmittance obtained for (orange curves) TM and (black curves) TE polarization and at normal incidence. (a-c) Vertical black lines denote λ_G and λ_R. (d) Photographs of the sample when illuminated with polarized white light at a decreasing angle (from left to right), showing a reflection with a coloration ranging from red (on the left) to green (on the right).

Optics EXPRESS

It's worth noting the good agreement in terms of spectral position of the peaks between the simulated spectra and those measured experimentally. However, especially for TM polarization, a reduction in the intensity and a slightly increased spectral width of the experimental peaks compared to numerical predictions is observed. The observed spectral broadening and reduction in peak intensity can be attributed to the presence of surface roughness on the SiN material and variations in the grating parameters across the sample. This phenomenon aligns with previous observations in sample fabrication, as documented in [56]. For both peaks, at both angles, and for both polarizations, the intensity, spectral position, and full width at half-maximum (FWHM) $\Delta\lambda$ of the peaks, both experimental and simulated, are provided in Table 3.

Table 3. Comparison of intensity, spectral position, and FWHM of the peaks near green and red, obtained both experimentally and numerically, for incident angles of 45° and 50° and for both polarizations

Pol.	θ_s [°]	Type	"green" peak			"red" peak		
			R. [%]	λ [nm]	Δλ [nm]	R. [%]	λ [nm]	Δλ [nm]
TM	45	m.	54	538	9	45	619	9
		s.	97	541	3	82	615	4
	50	m.	33	515	12	40	592	10
		s.	96	519	5	97	593	3
TE	45	m.	49	552	15	58	637	15
		s.	76	552	4	85	639	9
	50	m.	59	535	12	57	615	22
		s.	73	535	13	85	615	6

Figure 8(c) illustrates the comparison between experimental and simulated transmittances. It reveals a reduction in transmittance for both polarizations. To provide an assessment of this reduction, it is useful to calculate the overall transparency of the metasurface. This can be estimated as the ratio of the integral of an ideal unity transmittance to that of the measured or calculated transmittance of the metasurface within the spectral range of interest (400 nm–700 nm). For the TM (TE) polarization, there is a modification from a simulated transparency of 87% (84%) to an experimental value of 68% (58.5%), resulting in an overall reduction of 19% (25.5%).

Finally, in Fig. 8(d), three photographs of the sample are shown when illuminated with polarized white light at three different decreasing angles (from left to right). We observe that the reflected light exhibits highly saturated and vibrant coloration, transitioning from red (Fig. 8(d) on the left), to yellow (Fig. 8(d) in the middle), to green (Fig. 8(d) on the right).

4. Conclusion

In conclusion, we proposed the design, fabrication, and characterization of a metalens based on a transparent all-dielectric metasurface. The proposed structure exhibits multiple selective reflection peaks with experimental linewidths ranging from approximately 10 to 20 nm (numerical simulations suggest they can be reduced to 3 nm). These reflection peaks are achieved through the engineering of resonances in a single guided mode and can be precisely controlled to reflect a comb of intense and saturated coloured light, demonstrating for the first time the possibility to exploit multiple guided mode resonances in the visible spectrum. The underlying mechanism governing the operation of the metalens has been extensively discussed by studying its behaviour with respect to each geometric parameter. Additionally, we have presented an analytical numerical method for the rapid determination of the spectral positions of guided mode resonances. This method has been validated against numerical simulations using the RCWA method. We have introduced a cost function definition to aid in the search for bichromatic and trichromatic solutions,

Optics EXPRESS

with the potential for generalization to the polychromatic ones. The proposed cost function streamlines the optimization process for designing multi-wavelength metalenses. An experimental demonstration was obtained by comparing the measured reflection spectra with those obtained numerically for a bichromatic configuration. This characterisation was performed for both TE and TM motions considering a source inclined at 45° and 50°. The comparison showed very good agreement regarding the spectral position of the peaks and a moderate reduction in their intensity. Our future research efforts will focus on the fabrication of a second-generation of metasurface samples with larger areas, suitable for scalable manufacturing techniques such as nanoimprinting. Additionally, we will assess the metalens performance in terms of other critical parameters, including resolution, field of view, and eyebox, which are crucial for wearable augmented reality systems. Furthermore, we proposed AR near-eye display as a tool to alleviate mild to moderate cognitive impairments by presenting the user with visual information to support indoor navigation, home safety, communication, and decision-making. This structure can be valuable for the realisation of visual aids to support individuals with cognitive impairment.

Funding. Regione Puglia (BURP n. 52 of 16/06/2019, Notice 2/FSE/2020 n. 57 of 13/05/2019, POR Puglia 2014-2020, Priority Axis OT X, REFIN).

Acknowledgments. GM is supported by a grant from Regione Puglia "Research for Innovation" (REFIN). REFIN is an intervention co-financed by the European Union under the POR Puglia 2014-2020, Priority Axis OT X "Investing in education, training and professional training for skills and lifelong learning - Action 10.4 - DGR 1991/2018 - Notice 2/FSE/2020 n. 57 of 13/05/2019 (BURP n. 52 of 16/06/2019). The fabrication process realized in this work was done within the LAAS-CNRS cleanroom facilities, member of the national RENATECH platform network.

Disclosures. The authors declare no conflicts of interest.

Data availability. Data underlying the results presented in this paper are not publicly available at this time but may be obtained from the authors upon reasonable request.

References

1. J. Oeppen and J. W. Vaupel, "Demography: Broken limits to life expectancy," Science **296**(5570), 1029–1031 (2002).
2. P. Bach-y-Rita and S. W. Kercel, "Sensory substitution and the human-machine interface," Trends Cognit. Sci. **7**(12), 541–546 (2003).
3. C. F. Ross, "Sensory science at the human–machine interface," Trends Food Sci. Technol. **20**(2), 63–72 (2009).
4. A. T. Chen, A. K. Teng, J. Zhao, *et al.*, "The use of visual methods to support communication with older adults with cognitive impairment: A scoping review," Geriatric Nursing **46**, 52–60 (2022).
5. R. Y. C. Kwan, C. W. Kwan, P. P. K. Kor, *et al.*, "Cognitive decline, sensory impairment, and the use of audio-visual aids by long-term care facility residents," BMC Geriatr. **22**(1), 216 (2022).
6. R. Hervás, J. Bravo, and J. Fontecha, "An assistive navigation system based on augmented reality and context awareness for people with mild cognitive impairments," IEEE J. Biomed. Health Inform. **18**(1), 368–374 (2014).
7. G. A. Alshafeey, M. M. Lakulu, M. A. Chyad, *et al.*, "Augmented reality for the disabled: review articles," J. ICT Educ. **6**(0 SE-Articles), 46–57 (2019).
8. M. S. Bourgeois, "Evaluating memory wallets in conversations with persons with dementia," J. Speech Hear. Res. **35**(6), 1344–1357 (1992).
9. Wan-Zu D Chang and Michelle S Bourgeois, "Effects of visual aids for end-of-life care on decisional capacity of people with dementia," Am. J. Speech-Language Pathol. **29**(1), 185–200 (2020).
10. P. Papcun, E. Kajáti, and J. Koziorek, "Human machine interface in concept of industry 4.0," in *2018 World Symposium on Digital Intelligence for Systems and Machines (DISA)* (2018), pp. 289–296.
11. L. Abdi, F. Ben Abdallah, and A. Meddeb, "In-vehicle augmented reality traffic information system: a new type of communication between driver and vehicle," Procedia Comput. Sci. **73**, 242–249 (2015).
12. H. Kim and J. L. Gabbard, "Assessing distraction potential of augmented reality head-up displays for vehicle drivers," Hum. Factors **64**(5), 852–865 (2022).
13. I. E. Sutherland, "A head-mounted three dimensional display," in *Proceedings of the December 9-11, 1968, Fall Joint Computer Conference, Part I* (1968), pp. 757–764.
14. O. Cakmakci and J. Rolland, "Head-worn displays: a review," J. Display Technol. **2**(3), 199–216 (2006).
15. J. Rolland and O. Cakmakci, "Head-worn displays: the future through new eyes," Opt. Photonics News **20**(4), 20–27 (2009).
16. G.-A. Koulieris, B. Bui, M. S. Banks, *et al.*, "Accommodation and comfort in head-mounted displays," ACM Trans. Graph. **36**(4), 1–11 (2017).
17. C. P. Chen, L. Mi, W. Zhang, *et al.*, "Waveguide-based near-eye display with dual-channel exit pupil expander," Displays **67**, 101998 (2021).

Optics EXPRESS

18. D. Cheng, Y. Wang, C. Xu, *et al.*, "Design of an ultra-thin near-eye display with geometrical waveguide and freeform optics," Opt. Express **22**(17), 20705–20719 (2014).
19. C. P. Chen, Y. Cui, Y. Chen, *et al.*, "Near-eye display with a triple-channel waveguide for metaverse," Opt. Express **30**(17), 31256–31266 (2022).
20. J. Jeong, C.-K. Lee, B. Lee, *et al.*, "Holographically printed freeform mirror array for augmented reality near-eye display," IEEE Photonics Technol. Lett. **32**(16), 991–994 (2020).
21. T. Shu, G. Hu, R. Wu, *et al.*, "Compact full-color augmented reality near-eye display using freeform optics and a holographic optical combiner," Opt. Express **30**(18), 31714–31727 (2022).
22. S. Lan, X. Zhang, M. Taghinejad, *et al.*, "Metasurfaces for near-eye augmented reality," ACS Photonics **6**(4), 864–870 (2019).
23. D. N. Neshev and A. E. Miroshnichenko, "Enabling smart vision with metasurfaces," Nat. Photonics **17**(1), 26–35 (2023).
24. A. Maimone, D. Lanman, K. Rathinavel, *et al.*, "Pinlight displays: wide field of view augmented reality eyeglasses using defocused point light sources," in *ACM SIGGRAPH 2014 Emerging Technologies* (2014), p. 1.
25. G. Magno, A. Monmayrant, M. Grande, *et al.*, "Stable planar mesoscopic photonic crystal cavities," Opt. Lett. **39**(14), 4223 (2014).
26. G. Magno, M. Grande, A. Monmayrant, *et al.*, "Controlled reflectivities in self-collimating mesoscopic photonic crystal," J. Opt. Soc. Am. B **31**(2), 355 (2014).
27. G. Magno, O. Gauthier-Lafaye, G. Caló, *et al.*, "Mesoscopic self-collimation along arbitrary directions and below the light line," Opt. Express **27**(21), 30287 (2019).
28. B. Leroy, G. Magno, D. Barat, *et al.*, "Integrated plasmonic nanoantenna gratings for large area coherent optical source," in *Optics InfoBase Conference Papers, The European Conference on Lasers and Electro-Optics, CLEO_Europe_2019* (2019), Part F140-.
29. B. Gralak, H. Bertin, Y. Brûlé, *et al.*, "Design of optical metasurfaces for innovative display devices," in *Optics InfoBase Conference Papers, Optoelectronic Devices and Integration, OEDI_2019* (2019), Part F151-.
30. H. Bertin, Y. Brûlé, G. Magno, *et al.*, "Correlated disordered plasmonic nanostructures arrays for augmented reality," ACS Photonics **5**(7), 2661–2668 (2018).
31. H. Bertin, Y. Brûlé, G. Magno, *et al.*, "Periodic and disordered plasmonic nanostructures arrays for visualization application," in *Optics InfoBase Conference Papers, Asia Communications and Photonics Conference, ACPC* 2017 (2017), Part F83-A.
32. G. Magno, M. Fevrier, P. Gogol, *et al.*, "Strong coupling and vortexes assisted slow light in plasmonic chain-SOI waveguide systems," Sci. Rep. **7**(1), 7228 (2017).
33. G. Magno, B. Leroy, D. Barat, *et al.*, "Numerical demonstration of surface lattice resonance excitation in integrated localized surface plasmon waveguides," Opt. Express **30**(4), 5835–5847 (2022).
34. P. Dantonio, A. Vincenzo Inchingolo, G. Perna, *et al.*, "Localized surface plasmon resonances in gold nano-patches on a gallium nitride substrate," Nanotechnology **23**(45), 455709 (2012).
35. A. Ecarnot, G. Magno, V. Yam, *et al.*, "Ultra-efficient nanoparticle trapping by integrated plasmonic dimers," Opt. Lett. **43**(3), 455 (2018).
36. G. Magno, A. Ecarnot, C. Pin, *et al.*, "Integrated plasmonic nanotweezers for nanoparticle manipulation," Opt. Lett. **41**(16), 3679 (2016).
37. G. Magno, M. Grande, V. Petruzzelli, *et al.*, "High-efficient ultra-short vertical long-range plasmonic couplers," J. Nanophoton **6**(1), 061609 (2012).
38. G. Magno, M. Grande, V. Petruzzelli, *et al.*, "Asymmetric hybrid double dielectric loaded plasmonic waveguides for sensing applications," Sens. Actuators, B **186**, 148–155 (2013).
39. G. Magno, M. Grande, V. Petruzzelli, *et al.*, "Numerical analysis of the coupling mechanism in long-range plasmonic couplers at 155 µm," Opt. Lett. **38**(1), 46 (2013).
40. B. Dagens, M. Février, P. Gogol, *et al.*, "Direct observation of optical field phase carving in the vicinity of plasmonic metasurfaces," Nano Lett. **16**(7), 4014–4018 (2016).
41. M. Grande, M. A. Vincenti, T. Stomeo, *et al.*, "Graphene-based perfect optical absorbers harnessing guided mode resonances," Opt. Express **23**(16), 21032 (2015).
42. T. Zhan, Y.-H. Lee, G. Tan, *et al.*, "Pancharatnam–Berry optical elements for head-up and near-eye displays [Invited]," J. Opt. Soc. Am. B **36**(5), D52 (2019).
43. K. Falaggis, J. Rolland, F. Duerr, *et al.*, "Freeform optics: introduction," Opt. Express **30**(4), 6450–6455 (2022).
44. C. Hong, S. Colburn, A. Majumdar, *et al.*, "Flat metaform near-eye visor," Appl. Opt. **56**(31), 8822–8827 (2017).
45. D. K. Nikolov, A. Bauer, F. Cheng, *et al.*, "Metaform optics: Bridging nanophotonics and freeform optics," Sci. Adv. **7**(18), eabe5112 (2021).
46. S. S. Wang and R. Magnusson, "Theory and applications of guided-mode resonance filters," Appl. Opt. **32**(14), 2606–2613 (1993).
47. M. J. Uddin, T. Khaleque, and R. Magnusson, "Guided-mode resonant polarization-controlled tunable color filters," Opt. Express **22**(10), 12307–12315 (2014).
48. M. J. Uddin and R. Magnusson, "Highly efficient color filter array using resonant Si3N4 gratings," Opt. Express **21**(10), 12495–12506 (2013).

Optics EXPRESS

49. S. He, Z. Shi, X. Li, *et al.*, "Membrane guided-mode resonant color filters exhibiting adjustable spectral response," Opt. Commun. **342**, 129–135 (2015).
50. D. Wang, Q. Wang, and D. Liu, "Polarization-insensitive filter for incidence between classic and full conical mountings," IEEE Photonics Technol. Lett. **30**(5), 495–498 (2018).
51. D. Wang and Q. Wang, "Spectral features of guided mode resonant filter with two-dimensional crossed grating," J. Lightwave Technol. **37**(17), 4445–4450 (2019).
52. I. Allayarov, A. B. Evlyukhin, and A. Calà Lesina, "Multiresonant all-dielectric metasurfaces based on high-order multipole coupling in the visible," Opt. Express **32**(4), 5641–5658 (2024).
53. J.-P. Hugonin and P. Lalanne, "Light-in-complex-nanostructures/RETICOLO: V9," (2021).
54. T. K. Gaylord and M. G. Moharam, "Analysis and applications of optical diffraction by gratings," Proc. IEEE **73**(5), 894–937 (1985).
55. R. Soler and E. Voss, "Biologically relevant lighting: an industry perspective," Front. Neurosci. **15**, (2021).
56. A.-L. Fehrembach, O. Gauthier-Lafaye, K. C. S. Yu, *et al.*, "Measurement and modeling of 2D hexagonal resonant-grating filter performance," J. Opt. Soc. Am. A **27**(7), 1535–1540 (2010).